Lessons learned from UAV surveys over drifting sea ice at high latitudes

Niklas Neckel[1], Niels Fuchs[2], Jonathan Kolar[3], Thomas Kordes[1], and Christian Haas[1]

[1]Alfred-Wegener-Institut, Helmholtz-Zentrum für Polar- und Meeresforschung, Bremerhaven, Germany
[2]Institute of Oceanography, University of Hamburg, Germany
[3]Institute of Earth Sciences, University of Lausanne, Switzerland

Correspondence: Niklas Neckel (niklas.neckel@awi.de)

Abstract. In this study, we provide an overview of the challenges encountered when using Unmanned Aerial Vehicles (UAVs), or drones, for mapping high-latitude Arctic pack ice. A major challenge when generating void-free orthomosaics and Digital Elevation Models (DEMs) of ice floes is their drift, which can easily exceed 0.5 m s^{-1} in the central Arctic Ocean. To address this issue, we developed and evaluated a novel approach for conducting autonomous grid missions at high latitudes, incorporating ice-drift correction during both the pre-flight planning and post-flight processing stages. Although demonstrated using a DJI camera drone, the proposed workflow can be readily adapted to UAVs from other manufacturers. Using this approach, we generated drift-corrected orthomosaics and DEMs for all ice floes visited during the ArcWatch-2 expedition in August and September 2024 based on Structure from Motion (SfM) photogrammetry. In addition to the UAV camera system, we evaluated a drone-based laser scanner and incorporated measurements from drifting Global Navigation Satellite System (GNSS) stations for georeferencing and validation. Finally, we demonstrate the potential of drone-acquired data for estimating ice thickness, classifying surface types, and retrieving melt pond depths. These high-resolution observations enable the upscaling of *in situ* measurements and have the potential to improve estimates of sea-ice mass balance and meltwater distribution.

1 Introduction

In the future, Unmanned Aerial Vehicles (UAVs), or drones, may become a standard tool for sea-ice observations, offering a cost-efficient complement to helicopter-based systems with the capability to operate under weather conditions that might restrict helicopter flights for safety reasons. Furthermore many drones are pollution free, noiseless and easy to handle giving the opportunity to monitor the highly vulnerable polar environment in an adapted and less expensive way. While flying off-the-shelf drones over stable ground at mid latitudes is almost trivial, we encountered several problems over high Arctic drift ice for which we found solutions or give suggestions for upcoming expeditions. Problems range from icing and battery lifetime due to low temperatures to issues related to drifting ice floes and the inability to display the drone's position north of 85° N latitude. During the ArcWatch-2 *RV Polarstern* Expedition we had the opportunity to fly two off-the-shelf drone systems, namely a DJI Mavic 3 and a DJI Matrice 350 RTK over drifting sea ice. While the DJI Mavic 3 is a consumer grade camera drone, the DJI Matrice 350 RTK was equipped with a laser scanner to capture the surface topography of the ice. All drone surveys were carried out by authorized pilots in accordance with all applicable legal requirements.

The overarching research goal of the ArcWatch-2 cruise was a multidisciplinary, large-scale assessment of environmental changes in the central Arctic Ocean and on the Barents Sea continental slope (Rabe and Geibert, 2025). Between 2024-08-16 and 2024-09-26 the *RV Polarstern* was moored to 10 larger ice floes across the entire Arctic Ocean (ice stations, Tab. 1) giving the opportunity to test drone operations and to measure relevant sea ice parameters such as ice drift, ice thickness, ice/snow densities and meltpond depths. The acquired drone data were processed to orthomosaics and DEMs for all ice stations building a valuable dataset for all ice related work conducted during the expedition. Initial maps were generated in near-real time, i.e. while the vessel was still moored to the ice floe, supporting in-field decision-making and logistics. Building on this approach, we propose to routinely produce such high-resolution snapshots across different spatial and temporal scales throughout the Arctic Ocean during future cruises.

In-depth analyses of the acquired datasets enabled the derivation of melt pond depth and sea-ice thickness estimates from the DEMs, which were compared with simultaneously acquired *in situ* measurements. This is an important step towards up-scaling *in situ* observations of ice thickness and melt pond depth to the scale of entire ice floes, which is essential for improved mass balance estimates and for the development and parameterization of sea-ice models.

Table 1. List of ice stations visited during Arcwatch-2 including average geographic positions for the respective reference date and time.

Ice station	Date and time	Latitude	Longtitude
PS144_007_01_ICE01	2024-08-16 17:00:00	85.05805	42.93493
PS144_023_01_ICE02	2024-08-29 22:00:00	84.50036	115.72034
PS144_042_01_ICE03	2024-09-02 23:00:00	84.83094	128.87743
PS144_050_01_ICE04	2024-09-05 09:09:21	85.02579	139.94363
PS144_067_01_ICE05	2024-09-08 15:00:00	84.94667	162.09426
PS144_080_01_ICE06	2024-09-11 01:00:00	84.93331	179.41320
PS144_085_01_ICE07	2024-09-13 09:00:00	87.50035	178.72568
PS144_109_01_ICE08	2024-09-19 09:20:15	89.95154	-142.69616
PS144_123_02_ICE09	2024-09-23 10:00:00	88.07016	59.95280
PS144_134_01_ICE10	2024-09-26 06:00:00	87.04715	57.07384

2 Data and Methods

2.1 GNSS data

Depending on the duration of the ice station and safety restrictions we were able to install between 3 and 6 autonomous Global Navigation Satellite System (GNSS) stations per ice station serving as Ground Control Points (GCPs) for UAV surveys. These consist of one Novatel FlexPak6 L-Band GNSS receiver, one Novatel choke ring antenna, one data logger and one battery (Neckel et al., 2020). The antennas were mounted on the cases housing the GNSS receiver, data logger and battery. GNSS data were logged every 5 s and were processed employing the Canadian Spatial Reference System Precise Point Positioning

(CSRS-PPP) service (Tétreault et al., 2005). The processed GNSS data are referenced to the International Terrestrial Reference Frame 2020 (ITRF2020). Both raw and post-processed GNSS data for all ice stations visited during ArcWatch-2 are available at Neckel et al. (2025b). Next to each GNSS station we drilled through the ice and measured the local ice thickness and freeboard. Additionally, we manually measured the snow thickness and antenna height above the ice surface.

2.2 UAV camera flights

2.2.1 Flight preparation

To characterize the surface conditions at each ice station, we conducted both manual and autonomous photogrammetric surveys using a DJI Mavic 3 UAV equipped with a Hasselblad L2D-20C camera including a 4/3 CMOS sensor. Autonomous photogrammetric surveys over drifting sea ice at very high latitudes pose two general challenges that are independent of the UAV platform. First, mission planning at extreme latitudes is not supported by all commercial UAV systems. Second, the continuous ice drift during a survey must be accounted for to maintain the planned image overlap and ensure complete photogrammetric coverage. The methodology presented here addresses both challenges and is generally applicable to any UAV platform that supports waypoint-based autonomous missions. The DJI Mavic 3 served as the implementation platform for this study.

The proposed workflow consists of three platform-independent steps: (i) generation of a standard photogrammetric survey grid based on the desired camera geometry and flight parameters, (ii) automatic alignment of the survey grid with the research vessel using a user-defined offset and orientation, and (iii) transformation of the grid into an ice-fixed flight plan by correcting all waypoints for the expected ice drift during the survey. Only the final export of the corrected waypoints depends on the mission format supported by the UAV platform. In this study, the resulting mission was exported in the KMZ format required by the DJI waypoint system. Although demonstrated using the DJI Mavic 3, the workflow can be adapted to any waypoint-capable flight controller by modifying only the final mission export.

The initial survey grid was created using the QGIS *Flight Planner* plugin based on the camera focal length, sensor size, desired flight altitude, and image overlap. Flight parameters were selected to cover an area of approximately 600 m $\times$ 600 m using a flight speed of 10 m s^{-1}, an altitude of 100 m above the ice surface, and image overlaps of 80% and 60% along- and across-track, respectively. These settings resulted in a flight duration of approximately 20 minutes, well within the endurance limits of modern UAVs. The resulting camera positions were then processed using a custom Python application to translate and rotate the survey grid into an operational flight path at a user-specified distance parallel to the research vessel.

As sea ice is continuously drifting, the planned camera positions were corrected prior to each flight using drift vectors derived from 10-minute handheld GNSS observations acquired immediately before takeoff. During the ArcWatch-2 expedition, measured drift speeds ranged from 0.03 to 0.52 m s^{-1} (Fig. 1). Assuming constant drift over the flight duration, the planned waypoints were translated accordingly to generate an ice-fixed survey grid (Fig. 2a). Without this correction, the intended image overlap may not be maintained, potentially resulting in gaps in the final orthomosaics. When the vessel was moored to

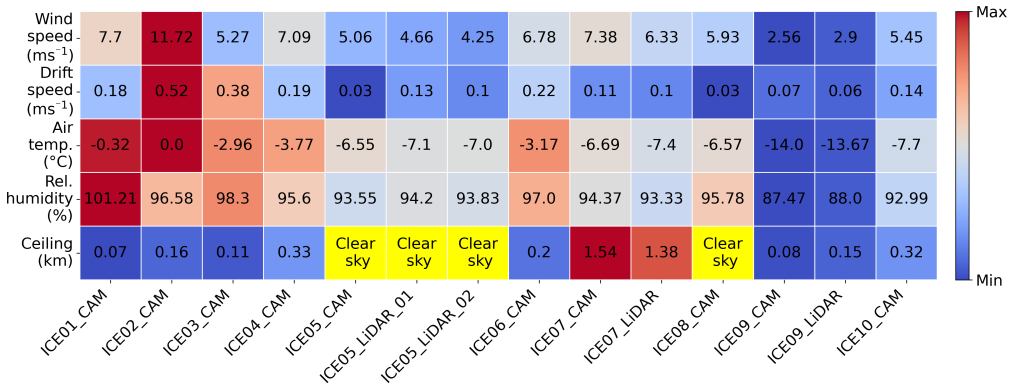


Figure 1. Environmental conditions at UAV surveys conducted during the ArcWatch-2 expedition. Here the average values of the listed parameters in the time of the respective UAV flight are shown. The x-axis is labeled by the ice station number with *CAM* for an UAV camera flight or *LiDAR* for an UAV LiDAR survey. The reference times of all ice stations are listed in Table 1. Colors are normalized to min-max of the respective variable.

an ice floe, the vessel's course and speed provided an equivalent estimate of ice drift, eliminating the need for separate handheld GPS measurements. An additional user-defined time offset was applied to account for the interval between drift estimation and UAV launch, ensuring that the corrected flight plan remained synchronized with the drifting ice.

The corrected waypoint file was subsequently exported in the controller-compatible KMZ format. With the exception of this platform-specific mission export, all steps of the workflow are independent of the UAV platform and can be applied to most drones supporting waypoint-based autonomous flights. The complete mission-planning workflow was implemented in Python and is publicly available via GitLab.

Before each flight, the camera exposure settings were adjusted manually according to the prevailing illumination and surface conditions. For the ArcWatch-2 campaign, images were acquired with a fixed aperture of f/2.8, ISO values between 100 and 400, and shutter speeds ranging from 1/640 to 1/1600 s. All images were stored simultaneously in DNG and JPG format on the UAV memory card.

2.2.2 Generation of Orthomosaics and Digital Elevation Models

Orthomosaics and DEMs were generated for all ice stations listed in Table 1. After an initial quality check, we used the images stored in JPG format on the memory card of the drone. Independent if the data were acquired manually or via our automatic grid flight routine, all images were drift-corrected to the reference time stamps listed in Table 1 (Fig. 2b). For this, we extracted the time and camera position from the Exchangeable Image File Format (EXIF) metadata of each image. We then selected one GNSS reference station and calculated the difference in meters between the position of the respective reference GNSS station at the reference time shown in Table 1 and at the acquisition time of each image. For the latter the GNSS data were interpolated to the exact acquisition time of the respective image. This estimate was used as an initial drift correction and has been proven mandatory elsewhere (Hyun et al., 2019; Neckel et al., 2023; Steer and Divine, 2024).

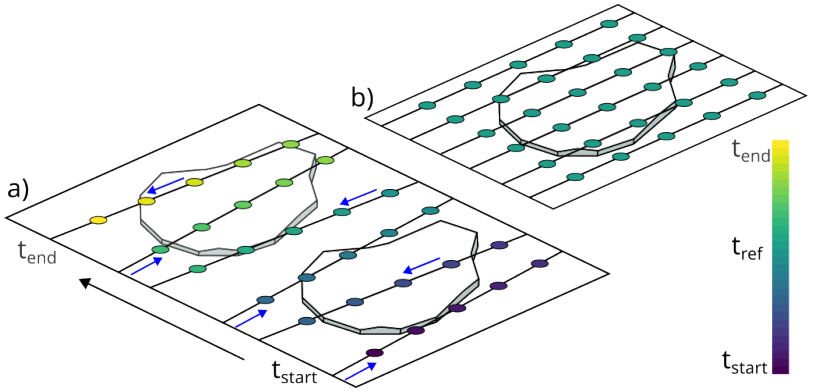


Figure 2. Scheme of pre- and post-flight drift correction of UAV camera grid flights. The ice drift (black arrow) is measured prior to the flight and is included in the mission planing, resulting in an ice-fixed grid mission **(a)**. Time is indicated by the color gradient and flight direction of the UAV by blue arrows. During post-processing, GNSS-based drift estimates are used to transform image locations to a common reference time and their corresponding geographic positions **(b)**.

The images including information on their drift-corrected locations and attitude angles were imported into the commercial Agisoft Metashape software (Agisoft LLC, 2021), as well as the GNSS-based GCPs at the reference times listed in Table 1 (the total number of GCPs per ice station is listed in Tab. 2). After the generation of tie points from the drift-corrected images, the choke ring antennas were selected in a couple of images and assigned to the nearest GCP. Then a camera optimization step was performed to improve the camera positions using the GCPs. In order to test the influence of GCPs on the accuracy of the final DEMs, we included 1) no GCPs, 2) 3 GCPs forming the largest triangle possible and 3) all GCPs in the photogrammetric processing (Tab. 2). In the successive step, a dense point cloud was generated, which was gridded to an individual DEM for each ice floe. If an overall elevation trend was observed in the derived DEM, we applied an additional fit to detrend the data (e.g. Drews et al., 2009; Landy et al., 2015). Depending on the shape of the elevation trend, we subtracted either a linear or a quadratic fitted surface from the DEM. In a last step, the single images were projected on the respective DEM and stitched to a final orthomosaic for each ice station.

2.2.3 Sea-ice surface properties retrieved from camera data

The implementation of drones aims to facilitate and expand studies of the ice surface and related processes. Therefore, we tested new algorithms recently developed for helicopter-borne systems using drone-acquired data. This includes an automatic pond detection with the classification algorithm PASTA-ice (Fuchs, 2023) and a melt pond depth retrieval (Fuchs et al., 2024). Due to the abundance of open melt ponds, we selected flight *ICE01_CAM* as a test case (Tab. 1 & Fig. 1). We first corrected the brightness of the RGB orthomosaic using an empirical line approach between manually determined points (Fig. 3a). Classification with PASTA-ice yields maps with every pixel assigned to a surface-type class, allowing for the derivation of areal melt pond fractions (e.g., 27% at ICE01) and vector polygons that encompass all adjacent pixels of similar types, such as a

single melt pond. Using these polygons, we determined the height of pond margins in the photogrammetrically derived DEM (Fig. 3b) and thus retrieved the height of the pond above sea level. With the correction for refraction at the air-pond interface, introduced in Fuchs et al. (2024), we derived the pond depth in a two-media photogrammetry approach (Fig. 3). In this process, deviations caused by refraction are suppressed in the reconstruction to such an extent that it is ultimately sufficient to multiply the water depth at each pond pixel by the refractive index between air and water.

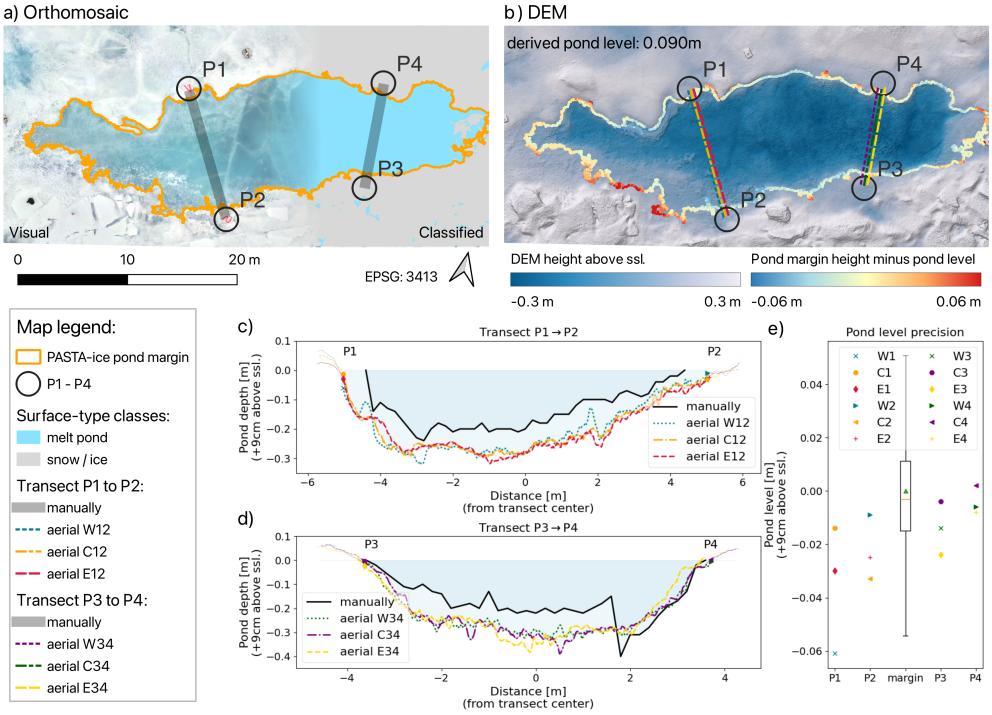


Figure 3. Sea-ice surface properties derived from UAV flight ICE01_CAM. Map of the ice surface around the main studied pond **a)**, showing the brightness corrected RGB orthomosaic on the left and the classification into main surface-type classes (grey: snow/ice, blue: ponds) on the right overlaid on the DEM. Example of pond depth retrieval including its vertical derivation from the mean pond level (**b**). Manual pond depth measurements along the two profile lines marked in **a)** and derived from the UAV data along three parallel lines at these locations (W, C, and E) are provided in panels **c)** and **d)** with water-filled area shaded in blue. Panel **e)** shows the estimated pond level at the transect pond edges from the mean pond level (markers) and along the entire pond margin (box and whiskers plot).

2.3 UAV Lidar flights

2.3.1 Flight preparation

The DJI Matrice 350 RTK drone was equipped with the Zenmuse L2 LiDAR module. The DJI Zenmuse L2 operates at a wavelength of 905 nm. This wavelength lies within the near-infrared region, where dry snow exhibits high reflectance, resulting in strong LiDAR return signals suitable for topographic mapping of snow- and ice-covered surfaces (Warren, 1982;

Deems et al., 2013). For flying the DJI Matrice 350 RTK drone with the Zenmuse L2 LiDAR module we needed to operate a DJI D-RTK 2 mobile base station on the aft corner of the helicopter pad from where also the UAV was launched manually. Before the actual scanning, an automatic calibration pattern was carried out by the flight system. The measurement itself consisted of a long straight line at a constant flight altitude between 100 m and 200 m. At the end of the survey, the system performed another automatic calibration pattern.

2.3.2 Generation of Digital Elevation Models

When employing DJI's L2 LiDAR module the user is forced to use DJI's Terra software for reading the acquired data. Data from the DJI D-RTK 2 mobile base station also needed to be available for the data acquisition period and imported into the software. LiDAR data were successfully acquired at ice stations ICE05, ICE07, and ICE09 and exported from the DJI Terra software in LAS (LASer) point cloud format, a standard file format for storing LiDAR point cloud data. We then applied a similar drift correction scheme as for the UAV camera data on the georeferenced point cloud data to match the reference date and time shown in Table 1. The drift-corrected point clouds were imported into the open CloudCompare software and referenced to the available GNSS derived GCPs. For ice station ICE05 data from two LiDAR flights were available (Fig. 1) and their point clouds were merged after referencing them to the available GCPs (Figs. 4c and d). Finally all point clouds were gridded to a spatial resolution of 0.15 m, resulting in a DEM for ice stations ICE05, ICE07 and ICE09. Similar to the photogrammetric DEMs, we removed slight elevation trends by subtracting either a linear or a quadratic fitted surface from the LiDAR-based DEMs.

2.4 Ice and snow thickness retrievals

During Arcwatch-2, ice thickness was measured directly by drilling and by sled based multi-frequency electromagnetic induction measurements (GEM-2, Geophex Ltd.) for all ice stations. While drill measurements result in the actual ice and snow thicknesses at a specific location, the GEM-2 measures the distance from the snow surface to the ice–ocean interface resulting in a total ice+snow thickness estimate (Itkin et al., 2023; Neudert et al., 2024). To retrieve the actual ice thickness, additional snow depth measurements were carried out along the GEM-2 transects employing a Magnaprobe device (Itkin et al., 2023). Both the GEM-2 and the Magnaprobe device record GNSS positions and timestamps which were used for a similar drift correction as for the drone data to match the reference date and time shown in Table 1. Both datasets were resampled onto a common track of equidistant measurement points having 1.5 m spacing, so that each point contained both snow and ice-thickness information (Kolar et al., 2025). Importantly, all GEM/Magnaprobe transects were conducted prior to the UAV flights. The clearly visible footpaths in the orthomosaics were used as reference features for minor manual horizontal adjustments of the GEM and Magnaprobe track data to improve their spatial alignment with the UAV-derived products.

As a case study, we converted both the photogrammetric and the LiDAR DEMs of ice station ICE05 into ice thickness estimates assuming hydrostatic equilibrium. The UAV-derived DEMs provide elevations relative to the ellipsoid. To obtain freeboard, we applied a constant vertical offset to each DEM such that the DEM elevation at one GNSS reference station matched the corresponding *in situ* freeboard measurement. This offset was then applied uniformly to the entire DEM to convert ellipsoidal

elevations into freeboard estimates. Furthermore, we used the average snow depth measured during the Magnaprobe survey, *in situ* measurements of ice and snow densities, and a fixed seawater density of 1023.9 kg m^{-3} to calculate ice thickness from freeboard.

3 Results

Photogrammetric DEMs and orthomosaics were generated for all 10 ice stations of the ArcWatch-2 expedition and are available through Neckel et al. (2025a). Table 2 summarizes the influence of different GCP configurations on the results, reporting the mean elevation residual and standard deviation (1σ) between the GCP elevations and the corresponding DEM elevations. Owing to the limited number of GCPs available at each ice station (3–6 points), all GCPs were included in the final DEM generation to maximize accuracy. Consequently, the reported residuals represent errors at the control points themselves and should not be interpreted as independent validation metrics. The largest scatter in the elevation residuals was observed at ICE07 and ICE09, where the standard deviations reached 0.23 and 0.21 m, respectively. Both sites were characterized by poor visibility and low surface contrast (Fig. 1, Tab. 2, Fig. 5c), which likely contributed to the reduced DEM accuracy. Under favorable conditions, standard deviations of the elevation residuals as low as 0.03 m were achieved (Fig. 1, Tab. 2, Fig. 5a).

Based on the photogrammetric DEMs we show results on melt pond depth retrievals for ice station ICE01, i.e. the only ice station with open melt ponds visited during the ArcWatch-2 expedition (Tab. 1 & Fig. 3). Comparing aerial with manually measured pond depths along two transect lines (P1-P2 and P3-P4) (Fig. 3c and d), reveals a highly variable pond bottom and a general overestimation of pond depth from the aerial approach by 6 cm on average. Due to the imprecise co-location of the transect, we extracted three closely spaced parallel lines (W, C, and E) from the aerial data. Most local features of the manual observations, except for a trench close to P4, are visible in at least one of these lines, highlighting the generally efficient retrieval. Inaccuracies in the reconstructed DEM and pond margin classification probably caused an overestimation of the pond level of up to 6 cm close to the transect points (Fig. 3e), contributing to the overall depth overestimation.

We further show the potential of photogrammetric and LiDAR DEMs for the derivation of freeboard and ice thickness assuming hydrostatic equilibrium (Fig. 4). Over flat ice areas where this assumption holds true, our results agree well with *in situ* drill and EM measurements. This is evident from Figure 4e where all measurements show average ice thicknesses between 1.2 and 1.3 m. Overall we found that UAV borne LiDAR has great potential and robust results could be obtained also in conditions were photogrammetric retrievals fail. When comparing the UAV LiDAR DEMs to the local GNSS reference measurements we obtain vertical accuracies between 0.02 and 0.15 m.

4 Discussion and Conclusion

Comparing the results from the different ice stations of the ArcWatch-2 expedition is challenging because environmental conditions, surface characteristics, and flight patterns varied between the visited ice floes. Nevertheless, the observations obtained during the ArcWatch-2 expedition allow us to identify several general conclusions for UAV operations over drifting sea ice at

Table 2. Influence of GCP configuration on UAV-derived DEM elevations. For each processing configuration (no GCPs, three GCPs, all GCPs, and, where applicable, an additional fitting step as described in Section 2.2.2), the Table reports the mean elevation residual between surveyed GCP elevations and the corresponding DEM elevations. The associated uncertainty is given as $\pm 1\sigma$, where σ is the standard deviation of the elevation residuals. Note that, due to the limited number of GCPs available at each ice station, some or all GCPs were included in the photogrammetric adjustment. Consequently, the reported values represent residual errors at the control points and should not be interpreted as independent validation metrics.

Station	No GCPs	Three GCPs	All GCPs (#)	Extra fit
ICE01*	16.98±0.16m	0.09±0.09m	0.09±0.07m (4)	-
ICE02*	6.06±0.15m	0.1±0.11m	0.02±0.03m (6)	-
ICE03*†	8.31±0.71m	0.13±0.14m	- (3)	0±0.03m
ICE04†	-14.74±1.01m	-1.26±1.36m	0.04±0.08m (6)	0±0.07m
ICE05†	-0.85±0.48m	0.03±0.12m	0.01±0.12m (6)	0±0.03m
ICE06†	8.56±0.74m	0.58±0.81m	0.07±0.14m (4)	0±0.05m
ICE07†	21.57±1.08m	1.52±1.22m	0.35±0.23m (6)	-
ICE08*	4.13±0.12m	0.04±0.11m	0.16±0.14m (5)	0±0.04m
ICE09†	16.39±0.53m	0.01±0.23m	0.04±0.21m (4)	-
ICE10†	20.88±2.06m	0.52±0.55m	0.13±0.04m (5)	-

* Manual flight, † Grid flight, # Number of GCPs

high latitudes.

Flying UAVs in Arctic conditions presents challenges for both the aircraft and the pilot. Low temperatures can reduce battery performance, while fog and high humidity can cause propeller icing, potentially leading to electric-motor overheating and flight termination. These issues highlight the importance of robust low-temperature operation and effective icing mitigation for UAV systems intended for polar fieldwork (Hann et al., 2021). In addition, the tested UAV systems and commercial software did not support the display or planning of positions north of 85° N. Although this limitation does not prevent the aircraft from flying, it makes conventional map-based mission planning difficult or impossible at the highest latitudes. The proposed mission-planning workflow provides a practical solution to this problem and, apart from the final mission export, is independent of the UAV platform.

The UAV camera flights can be separated into manual flights and autonomous grid flights, with the latter incorporating a priori ice-drift information into the flight planning (Fig. 2). Autonomous grid flights are particularly efficient for covering large areas. They enable the generation of orthomosaics of entire ice floes while minimizing flight time and redundant overpasses. Our results demonstrate that drift correction is essential during both mission planning and post-processing. This maintains the intended survey geometry and ensures spatially consistent products. In contrast, manual flights provide greater flexibility in selecting viewing directions and image acquisition geometry. This is advantageous when accurate three-dimensional reconstruction is required, for example for melt pond depth or freeboard retrievals. The lower vertical residuals obtained for several manual flights compared with grid flights (Tab. 2) suggest that image acquisition from multiple viewing directions can

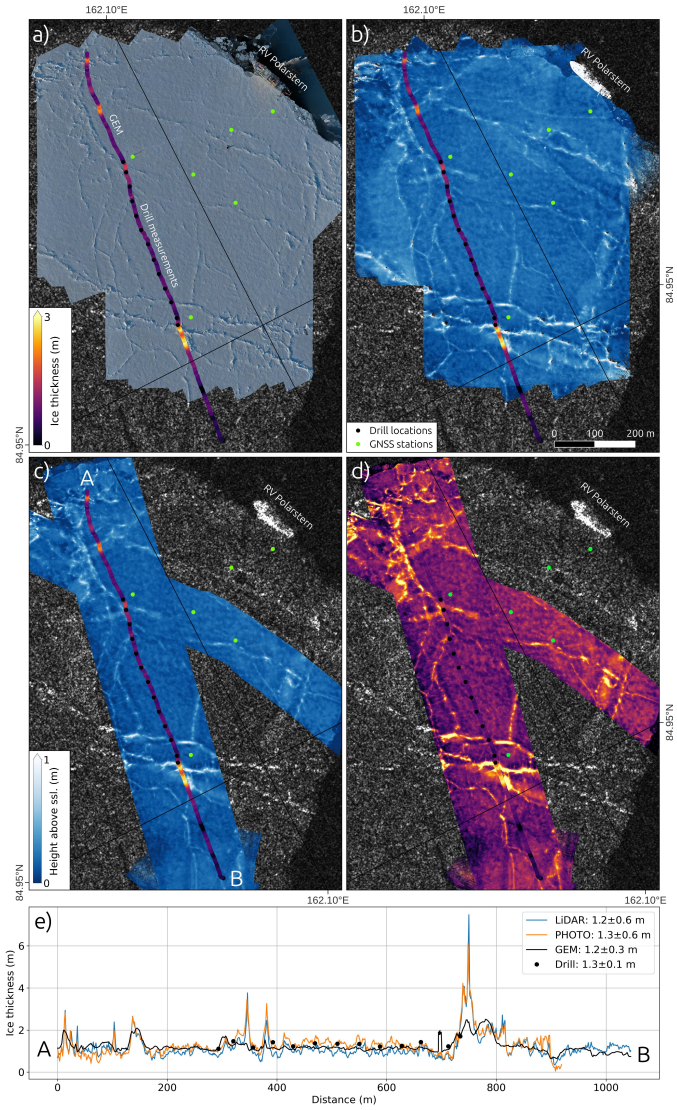


Figure 4. Results of UAV flights on 2024-09-08 (ICE05). Clear sky conditions and low ice drift (0.03 – 0.13 m s^{-1}) made this ice station ideal for drone operations. Orthomosaic and photogrammetric DEM are shown in panel **a)** and **b)** respectivley. LIDAR drone flights 5.1 and 5.2 are shown in panel **c)** while panel **d)** shows the inferred ice thickness estimates from the LiDAR flights. All maps are superimposed on a COSMO-SkyMed SAR image acquired on 2024-09-08 at 07:38:14 UTC and translated to the reference time shown in Table 1 (COSMO-SkyMed Product - ©ASI - Agenzia Spaziale Italiana - 2024). Ice thickness estimates are shown along the GEM profile A – B in panel **e)**.

be beneficial for detailed terrain reconstruction. Future autonomous surveys could combine the efficiency of grid flights with additional cross-grid or oblique image acquisitions (Elias et al., 2024). However, all flight paths must be adjusted for ice drift to remain in an ice-fixed reference frame.

The quality of the photogrammetric reconstruction was strongly affected by illumination and surface texture. At ICE07 and

ICE09, fog and diffuse illumination over relatively uniform snow and ice surfaces resulted in insufficient tie points and comparatively poor DEM quality (Fig. 1, Tab. 2, Fig. 5c). Under favorable conditions, however, vertical residuals as low as 0.03 m were achieved (Fig. 5a). These results demonstrate both the potential and the limitations of camera-based UAV mapping in the Arctic. Active LiDAR sensors, on the other hand, can provide an important complement under conditions in which passive photogrammetry becomes unreliable. The DJI Zenmuse L2 produced useful surface reconstructions at ICE07 and ICE09 despite the poor visibility. However, its dependence on a nearby base station limits its applicability to rapidly drifting sea ice. In addition, the raw data require processing through the DJI Terra software, limiting the possibilities for user-controlled drift correction. For future applications, LiDAR systems that can operate independently of a nearby base station and provide open access to raw data would therefore be advantageous.

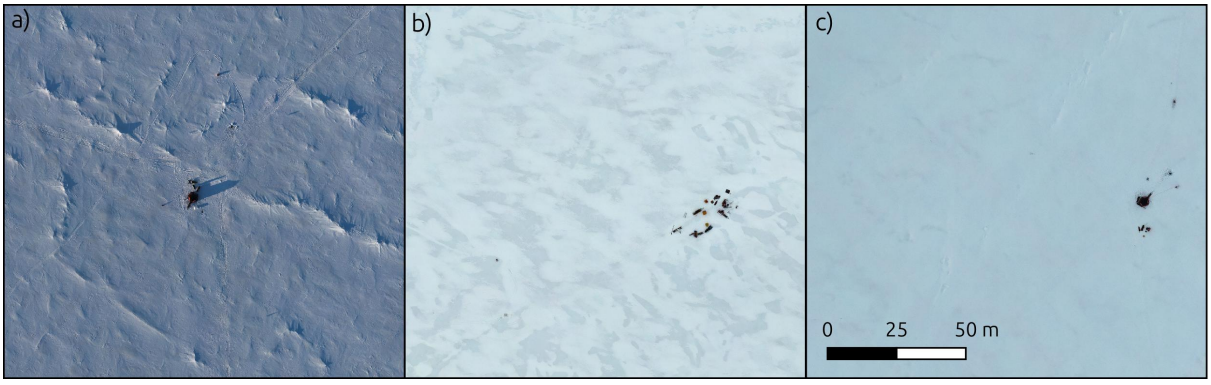


Figure 5. Varying lighting and surface conditions during the ArcWatch-2 expedition. Excellent conditions on 2024-09-08 (ICE05, **a**) with direct sunlight illuminating a ridged surface. Moderate conditions on 2024-09-11 (ICE06, **b**) with a low cloud ceiling over a snow/ice surface. Poor conditions on 2024-09-13 (ICE07, **c**) with diffuse lighting over a uniform snow surface. All panels are shown at the same scale.

As a case study, we also evaluated the potential of UAV-derived DEMs for retrieving sea-ice surface properties. Comparing the melt pond depth retrieval at ICE01 with *in situ* measurements, we observe an overestimation of 6 cm in the aerially derived pond depths, particularly in their absolute values, while the general gradients are correctly reconstructed (Fig. 3). The deviation exceeds previous evaluations that were based on earlier-season melt-pond observations (Fuchs et al., 2024). A plausible driver for this behavior is the increased translucency of the pond ice toward the end of the melt season. Stronger radiative transmission can reduce the optical visibility of the pond–ice interface in the image data. In particular, if the ice becomes more permeable, internal scatterers, like air inclusions, may be lost or their scattering efficiency may decrease, so that the photogrammetric reconstruction may instead latch onto optical features located deeper in the ice. Such a mechanism would readily explain a systematic offset in the absolute aerial pond depth, while leaving the overall gradient pattern largely intact, consistent with our observations. Based on these observations, we recommend further comparisons of the same ponds over the entire melt season, including an analysis of the actual reconstructed layer. Other sources of error may have contributed to the observed discrepancy between measured and retrieved pond depth. These include an imperfect pond-level determination, either because of steeper pond walls late in the season (Fetterer and Untersteiner, 1998) or due to horizontal inaccuracies in determining where the ice

is water-covered in the high-resolution image data. In addition, the spatial co-location of the in situ measurements appears imprecise. This could be improved in future campaigns by employing a tachymeter. Future UAV deployments during upcoming field campaigns will enable us to better quantify how retrieval errors depend on pond evolution and morphology, as well as on the specific sensing technology employed.

In addition to the melt pond depth retrieval, the UAV-derived DEMs were used to estimate freeboard and, subsequently, ice thickness. However, the validation of the freeboard and ice-thickness estimates is limited by the availability of independent *in situ* measurements. Freeboard measurements were only available at the GNSS stations, preventing a direct assessment of how the freeboard uncertainty varies with distance from these reference points. For the resulting ice-thickness estimates, the comparison with GEM-derived ice thickness along the GEM transect (Fig. 4e) provides an indirect assessment of the retrieval performance. Along the transect, the LiDAR- and photogrammetry-derived ice thicknesses differ from the GEM measurements by -0.06$\pm$0.46 m and 0.06$\pm$0.47 m, respectively (mean $\pm$ standard deviation). The small mean differences indicate that neither method exhibits a substantial systematic bias relative to the GEM measurements. However, the relatively large standard deviations demonstrate that local deviations can be considerable and provide a first quantitative indication of the retrieval variability. In particular, larger discrepancies are observed in heavily ridged regions, where the assumption of hydrostatic equilibrium is less well satisfied and the conversion from freeboard to ice thickness becomes less reliable. Consequently, the reported standard deviations should not be interpreted as spatially homogeneous uncertainty estimates, but rather as an indication of the range of deviations encountered in the available validation case. A more comprehensive assessment of the retrieval uncertainty would require independent freeboard and ice-thickness measurements spatially distributed throughout the surveyed area.

4.1 Lessons learned and recommendations

Based on our experience, several practical recommendations can be derived for future UAV surveys over drifting sea ice:

1. **Account for ice drift during both flight planning and post-processing.** Pre-flight drift correction preserves the intended survey geometry and image overlap, while post-flight correction transfers the acquired data to a common reference time. If the research vessel is moored to the surveyed ice floe, its course and speed can provide a direct estimate of ice drift and can be used for mission planning.

2. **Do not rely exclusively on commercial mission-planning interfaces at high latitudes.** Commercial software may lack map coverage or mission-planning functionality close to the pole, as these regions are not a primary focus of commercial mapping services. An externally generated waypoint mission provides a flexible solution and can be adapted to many UAV platforms.

3. **Use grid flights for efficient area coverage, but multiple viewing directions for detailed 3-D reconstruction.** Drift-corrected grid flights are well suited for large-area orthomosaics, whereas manual or more complex autonomous flight patterns with multiple viewing directions are preferable when accurate surface elevation is required for secondary products such as freeboard or melt pond depth retrievals.

4. **Consider LiDAR sensors as a complement to photogrammetry.** LiDAR can remain effective under poor visibility and low surface contrast, conditions under which passive photogrammetry may fail. However, the operational requirements of the LiDAR system, particularly those related to positioning, must be compatible with the expected ice drift and latitude.

5. **Prioritize robust operation under Arctic environmental conditions.** Low temperatures, fog, humidity, and icing can affect both aircraft performance and flight safety. Battery systems and sensing systems should therefore be designed or adapted for low-temperature operation and icing mitigation.

6. **Prefer open data policies.** Access to raw positioning and sensor data is particularly important over drifting sea ice. Processing chains should allow users to perform independent drift corrections, georeferencing, and quality control rather than requiring proprietary software for essential processing steps.

These lessons also suggest a set of requirements for future UAV systems intended for high-latitude sea-ice observations. An ideal system would provide reliable map display and waypoint planning at extreme latitudes, allow drift-aware flight planning, and provide open access to positioning and sensor data. Robust operation at low temperatures and under icing conditions would improve reliability, while open data formats would facilitate independent post-processing and integration with other observations.

Overall, our results demonstrate that UAVs can provide high-resolution observations of drifting sea ice over spatial scales that are difficult to capture with conventional *in situ* measurements. The combination of drift-corrected autonomous photogrammetry, complementary LiDAR observations, and GNSS-based georeferencing enabled the generation of consistent surface products across a wide range of Arctic environmental conditions. While some limitations encountered during the ArcWatch-2 expedition were specific to the employed DJI systems, the underlying challenges of ice drift, polar mission planning, limited surface contrast, icing, and georeferencing are common to UAV operations in the high Arctic. Addressing these challenges through platform-independent workflows and improved UAV capabilities will facilitate more efficient and reliable observations of sea-ice surface properties and support the upscaling of *in situ* measurements to the scale of entire ice floes.

Code availability. The python code for generating drift-corrected UAV survey grids is available at https://gitlab.awi.de/nneckel/MAVIC3GRID.

Data availability. The derived GNSS data are available at https://doi.pangaea.de/10.1594/PANGAEA.983769. The final orthomosaics and DEMs are available at https://doi.org/10.1594/PANGAEA.984115. The ice thickness data for all ice stations are available at https://doi.org/10.1594/PANGAEA.984304.

Author contributions. Niklas Neckel developed and tested the drift-correction scheme and wrote the initial manuscript draft. Niels Fuchs contributed to the calculation of pond depth and wrote the corresponding section. Jonathan Kolar contributed to the fieldwork and assisted

with processing the GEM-2 data. Thomas Kordes contributed the three LiDAR flights. Christian Haas supervised the study and contributed to writing and editing the manuscript.

Competing interests. The authors declare no competing interests

Acknowledgements. We thank Benjamin Rabe, Walter Geibert, Janna Rückert, Jonathan Bahlmann, Linnea Bühler, Nils Risse and the entire crew of the ArcWatch-2 expedition for their help in the field. We further thank Thomas Krumpen for his support from back home and Angelika Humbert for providing 6 GNSS stations.

References

Agisoft LLC (2021). Agisoft Metashape User Manual Professional Edition, Version 1.7.

Deems, J. S., Painter, T. H., and Finnegan, D. C. (2013). Lidar measurement of snow depth: a review. *Journal of Glaciology*, 59(215):467–479.

Drews, R., Rack, W., Wesche, C., and Helm, V. (2009). A Spatially Adjusted Elevation Model in Dronning Maud Land, Antarctica, Based on Differential SAR Interferometry. *Geoscience and Remote Sensing, IEEE Transactions on*, 47(8):2501–2509.

Elias, M., Isfort, S., Eltner, A., and Maas, H.-G. (2024). UAS Photogrammetry for Precise Digital Elevation Models of Complex Topography: A Strategy Guide. *ISPRS Annals of the Photogrammetry, Remote Sensing and Spatial Information Sciences*, X-2-2024:57–64.

Fetterer, F. and Untersteiner, N. (1998). Observations of melt ponds on Arctic sea ice. *Journal of Geophysical Research: Oceans*, 103(C11):24821–24835.

Fuchs, N. (2023). A multidimensional analysis of sea ice melt pond properties from aerial images.

Fuchs, N., von Albedyll, L., Birnbaum, G., Linhardt, F., Oppelt, N., and Haas, C. (2024). Sea ice melt pond bathymetry reconstructed from aerial photographs using photogrammetry: a new method applied to MOSAiC data. *The Cryosphere*, 18(7):2991–3015.

Hann, R., Enache, A., Nielsen, M. C., Stovner, B. N., van Beeck, J., Johansen, T. A., and Borup, K. T. (2021). Experimental Heat Loads for Electrothermal Anti-Icing and De-Icing on UAVs. *Aerospace*, 8(3).

Hyun, C.-U., Kim, J.-H., Han, H., and Kim, H.-c. (2019). Mosaicking Opportunistically Acquired Very High-Resolution Helicopter-Borne Images over Drifting Sea Ice Using COTS Sensors. *Sensors*, 19(5).

Itkin, P., Hendricks, S., Webster, M., von Albedyll, L., Arndt, S., Divine, D., Jaggi, M., Oggier, M., Raphael, I., Ricker, R., Rohde, J., Schneebeli, M., and Liston, G. E. (2023). Sea ice and snow characteristics from year-long transects at the MOSAiC Central Observatory. *Elementa: Science of the Anthropocene*, 11(1):00048.

Kolar, J., Neckel, N., Rückert, J. E., Bühler, L., Bahlmann, J., Risse, N., Hendricks, S., and Neudert, M. (2025). Ice and snow thickness measurements from the ArcWatch-2 Expedition.

Landy, J. C., Isleifson, D., Komarov, A. S., and Barber, D. G. (2015). Parameterization of Centimeter-Scale Sea Ice Surface Roughness Using Terrestrial LiDAR. *IEEE Transactions on Geoscience and Remote Sensing*, 53(3):1271–1286.

Neckel, N., Fuchs, N., Birnbaum, G., Hutter, N., Jutila, A., Buth, L., von Albedyll, L., Ricker, R., and Haas, C. (2023). Helicopter-borne RGB orthomosaics and photogrammetric digital elevation models from the MOSAiC Expedition. *Scientific Data*, 10(1):426.

Neckel, N., Fuchs, N., Kolar, J., Kordes, T., and Haas, C. (2025a). UAV based orthomosaics and ice surface models from the ArcWatch-2 Expedition.

Neckel, N., Kolar, J., Bühler, L., Bahlmann, J., Rückert, J. E., Trace-Kleeberg, S., and Risse, N. (2025b). GNSS measurements of PS144 ice stations.

Neckel, N., Zeising, O., Steinhage, D., Helm, V., and Humbert, A. (2020). Seasonal Observations at 79°N Glacier (Greenland) From Remote Sensing and in situ Measurements. *Frontiers in Earth Science*, 8.

Neudert, M., Arndt, S., Hendricks, S., Hoppmann, M., Schulze, M., and Haas, C. (2024). Improved sub-ice platelet layer mapping with multi-frequency EM induction sounding. *Journal of Applied Geophysics*, 230:105540.

Rabe, B. and Geibert, W. (2025). The Expedition PS144 of the Research Vessel POLARSTERN to the Arctic Ocean in 2024.

Steer, A. and Divine, D. (2024). Sea ice stations orthophotos and digital elevation models from drone -based aerial surveys conducted during Nansen Legacy cruises to the northern Barents Sea and the area north of Svalbard in 2021-2022.

Tétreault, P., Kouba, J., Héroux, P., and Legree, P. (2005). CSRS-PPP: An internet service for GPS user access to the Canadian Spatial Reference frame. *Geomatica*, 59:17–28.

Warren, S. G. (1982). Optical properties of snow. *Reviews of Geophysics*, 20(1):67–89.